

Binary Phase Diagram of the Manganese Oxide–Iron Oxide System

Jarrold V. Crum[†], Brian J. Riley, and John D. Vienna

Pacific Northwest National Laboratory, Richland, WA 99354

The phase equilibrium of the MnO_x – FeO_y binary system was measured within a temperature range of 750°–1590°C in air to examine inconsistencies found in literature, i.e., discrepancies related to the boundary between the spinel and hausmannite+spinel phase fields. Several studies are available in the literature that describe this boundary however the results and methods by which they were studied vary namely in terms of the atmosphere (air versus reducing) used and heat treatment/analysis methods. In addition, samples in the discrepancy region of the diagram revert to the hausmannite phase spontaneously upon cooling due to a displacive transformation. In order to accurately measure the phase boundaries, the following measurement methods were used: isothermal heat treatments followed by rapid quenching (in air or water), dilatometry, differential thermal analysis with thermogravimetric analysis, as well as room temperature and hot-stage X-ray diffraction (XRD). Phase assemblage(s) in each specimen were determined by XRD. Data were compared with literature and a new, self consistent phase diagram was developed. The results are reported along with background information and a comparison with previously reported data. This study will support development of a model for thermodynamic equilibria in complex, multioxide silicate melts.

I. Background

A MODEL for thermodynamic equilibria in complex multioxide silicate melts is being developed by a team of researchers from Oak Ridge National Laboratory, Pacific Northwest National Laboratory, and Pennsylvania State University for use in development of work for nuclear waste vitrification studies.¹ During the development of this model, which was based on the associate species model, inconsistencies were found with various literature values for phase equilibria in the MnO_x – FeO_y –air system.^{2–5} This study was undertaken to examine data from literature and measure phase equilibria in the MnO_x – FeO_y –air system to develop a single, self consistent data set for use in model development. Muan and Somiya³ performed the most thorough investigation of the Mn–Fe–O system in air. They were able to determine most of the phase boundaries; however, the hausmannite-to-spinel boundary was estimated because of measurement difficulties. Muan and Somiya³ did not provide a specific explanation regarding the methods by which data were obtained for this portion of the diagram, but there is mention of the instability of spinel upon cooling for compositions $>70\%$ MnO_x (on a Mn_2O_3 weight basis). In previous studies,^{2,4–7} researchers have specifically studied the tetragonal distortion of the cubic structure for compositions with high MnO_x concentrations in various atmospheres. Their work determined the compositional boundary where the transition from cubic structure to the

distorted tetragonal structure takes place. Upon cooling/quenching from the spinel phase field, spinel spontaneously converted to hausmannite due to a displacive transformation.⁸

In this study, all areas of the phase diagram from the melting temperature down to 750°C were investigated in air. Because this study was conducted in air, the oxidation state of Mn and Fe varied as a function of temperature. However, for ease of reading, all compositions are given in terms of MnO_x and FeO_y . *In situ* measurement techniques were used to measure the spinel phase field because of the reverting nature of compositions >65 wt% Mn_2O_3 from the high-temperature spinel (cubic) structure to the lower temperature hausmannite phase (tetragonal) structure upon cooling. All other aspects of the phase diagram were then compared mainly with the diagram by Muan and Somiya done in air along with other data from literature and a new phase diagram was generated.^{2–6}

II. Experimental Procedure

With the expectation of the reduction of Mn^{4+} to Mn^{3+} during treatment, 50 g batches were weighed accordingly from reagent grade Fe_2O_3 and MnO_2 to the nearest mg (± 0.002 mass%). The compositions of the mixtures batched included of $(\text{MnO}_x)_n$ $(\text{FeO}_y)_{(100-n)}$ where $n = 0, 5, 8, 10, 12, 20, 30, 40, 43, 50, 60, 65, 70, 80, 90, 95,$ and 100. First, compositions were equally spaced across the diagram at 10 mass% intervals. Additional compositions were added during the study to further refine the boundary locations in the diagram. Mixtures were homogenized using an agate milling chamber consisting of a cylindrical chamber with a matching puck. The chamber was placed in a vibratory fixture that rapidly shook the chamber and puck for 5 min. The mixtures were then baked at 1000°C inside of alumina crucibles for 24 h to react the two oxides, in a similar fashion to experimental methods used by Muan and Somiya.³ Subsamples of the reacted powders were then heat treated by one or more of the following methods: isothermal heat treatments (IHT) followed by rapid quenching in air or water (quench furnace [QF]), short-duration (0.5–4 h) IHTs for determining the melting point in alumina (TMP/Al) or platinum-alloy crucibles (TMP/Pt), dilatometry, differential thermal analysis with thermogravimetric analysis (DTA–TGA), as well as room temperature (X-ray diffraction [XRD]) and hot-stage X-ray diffraction (HSX). The average precision of these methods $\pm 5^\circ\text{C}$.

(1) Subsolidus Measurements

Reactions from one solid phase to another in this binary system occurred anywhere from fractions of a second to >250 h. For this reason, all methods were used in the subsolidus regions.

The majority of specimens were studied using the IHT method with heat treatment in a Deltech[®] (Deltech Inc., Denver, CO) uniform temperature furnace for a minimum of 72 h, air or water quenched to room temperature, and then examined using the XRD method. IHT samples were loaded into an alumina crucible at ~ 2 –3 g per sample and, depending their phase field, were either heated to a temperature of interest and then held for the duration of the heat treatment or they were initially soaked at a higher temperature (1300°–1400°C) for 2 h, then cooled by changing the furnace set point to the temperature of interest and

T. A. Vanderah—Contributing editor

Manuscript No. 25843. Received February 4, 2009; approved May 27, 2009.

A portion of the research was performed using EMSL, a national scientific user facility sponsored by the Department of Energy's Office of Biological and Environmental Research located at Pacific Northwest National Laboratory. Pacific Northwest National Laboratory is operated for the U.S. Department of Energy by Battelle under Contract DE-AC05-76RL01830.

[†]Author to whom correspondence should be addressed. e-mail: jarrod.crum@pnl.gov

allowing the furnace to rapidly cool at a rate $>10^{\circ}\text{C}/\text{min}$, and held for the duration of the heat treatment. This was done only for samples used to determine the boundaries were oxidation begins, i.e. $(\text{Mn},\text{Fe})_3\text{O}_4$ to $(\text{Mn},\text{Fe})_2\text{O}_3$ oxidation reaction. The initial 2 h soak at $1300^{\circ}\text{--}1400^{\circ}\text{C}$ was used to fully reduce the samples to a single phase of $(\text{Mn},\text{Fe})_3\text{O}_4$ (spinel) before lowering the heat-treatment temperature down to the temperature of interest to insure the boundary was approached from a higher temperature (reduced $(\text{Mn},\text{Fe})_3\text{O}_4$) and avoid difficulties related to reducing a trace amount of $(\text{Mn},\text{Fe})_2\text{O}_3$ at the $(\text{Mn},\text{Fe})_3\text{O}_4$ (spinel)– $(\text{Mn},\text{Fe})_2\text{O}_3$ (hematite, bixbyite, respectively) boundaries.

Room temperature XRD measurements were performed with a Scintag PAD V diffractometer (Thermo Fischer Scientific Inc., Waltham, MA) using $\text{CuK}\alpha$ radiation ($\lambda = 1.5406 \text{ \AA}$) at 45 kV and 40 mA equipped with a Peltier-cooled Si(Li) solid-state detector. The experiments were done using $\theta/2\theta$ geometry in a step-scan approach from 5° to $75^{\circ} 2\theta$ with a step size of $0.04^{\circ} 2\theta$ and a dwell time of 6 s per step. Jade 6[®] software was used to process and identify phase assemblages.

Samples examined by DTA–TGA were done so using a TA instruments SDT 2960 run in air. Samples ($\sim 75\text{--}150 \text{ mg}$) were placed in a platinum crucible and heated at various heating rates through a temperature range that encompassed all of the expected phase changes.

Samples near the high MnO_x side of the diagram ($n = 80\text{--}100$) were examined *in situ* by HSX using a Philips X'Pert MPD PW3040/00 system (PANalytical Inc., Westborough, MA) equipped with an Anton-Paar HTK 1200 hot-stage with a $\text{CuK}\alpha$ X-ray source, because of the reverting nature of spinel to hausmannite upon cooling for IHT specimens. Hot-stage samples were ramp heated at $5^{\circ}\text{C}/\text{min}$ from room temperature to the temperatures of interest where they were held for one hour before scanning the sample. Then the samples were cooled at the same rate and held at temperatures of interest for 1 h before scanning. Scans were done within 10°C above and below each suspected phase change.

One composition, $(\text{MnO}_x)_n(\text{FeO}_y)_{20}$, was examined using a Linseis L70/2171 differential dilatometer (Linseis Inc., Robbinsville, NJ) to identify phase changes by variances in thermal expansion rates as a function of temperature. This method was used for this sample because as the concentration of Mn decreased it resulted in decreased signal strength of the exothermic reaction from hausmannite to spinel on the DTA–TGA. The sample was uniaxially pressed into a bar at 60 kpsi using an isostatic press, pre-fired at 1200°C , cut into a bar with dimensions of $25 \text{ mm} \times \sim 3 \text{ mm} \times \sim 5 \text{ mm}$, and then was heated at a rate of $1^{\circ}\text{C}/\text{min}$ up to 1200°C , held for 1 h, and cooled back to room temperature. A second sample was heated at a rate of $0.5^{\circ}\text{C}/\text{min}$ up to 1250°C and cooled back down to room temperature.

(2) Liquidus Boundary Measurements

Subsamples of each mixture were used for heat treatments at various temperatures in alumina (TMP/Al) and platinum-alloy (Pt-10%Rh) (TMP/Pt) crucibles near the melting points published in the literature.^{3,9} Reactions from solid phase to a liquid occur in a matter of minutes. For this reason, samples were generally isothermally heat treated in intervals between 0.5 and 4 h followed by rapid quenching in air. Following heat treatment intervals, specimens were visually examined for evidence of melting dictated by a reflective surface. A series of mixtures were measured side by side in both Pt-10%Rh crucibles and alumina crucibles to determine if alumina has a significant effect on the liquidus boundary measurements. Backscattered scanning electron microscopy (SEM) and energy dispersive spectroscopy (EDS) were performed on a cross-sectioned specimen melted in an Al_2O_3 crucible in order to determine the interaction of the sample with the crucible.

III. Results

The phases determined using XRD included hematite (Fe_2O_3), bixbyite [$(\text{Fe}^{3+}, \text{Mn}^{3+})_2\text{O}_3$], spinel (solid solution of jacobsite/iwakiite/magnetite) [$(\text{Fe}^{2+}, \text{Mn}^{2+})(\text{Fe}^{3+}, \text{Mn}^{3+})_2\text{O}_4$], and hausmannite [$(\text{Mn}^{2+})(\text{Mn}^{3+})_2\text{O}_4$]. XRD powder diffraction files used for identification were the following: ICDD 33-0664 (hematite), ICSD 75-0894 (bixbyite), ICSD 74-2403 (jacobsite), and ICDD 24-0734 (hausmannite). All data used in assembling the phase diagram presented in Fig. 1 are also given in Table I. Different phases are denoted by the following symbols: “L” for liquid, “T” for hausmannite (tetragonal), “B” for bixbyite, “S” for spinel, “H” for hematite, and mixtures of these.

An overwhelming majority of the samples were measured using the IHT and XRD methods in order to determine phase assemblage. Most of the samples analyzed using the IHT method resulted in identification of distinct boundaries. Figure 2 shows XRD patterns collected for the mixture $(\text{MnO}_x)_{20}(\text{FeO}_y)_{80}$, at 1301° , 1200° , and 965°C which correspond to the phase fields of spinel, spinel+hematite, and hematite+bixbyite, respectively. Some boundary determinations were complicated by the lingering appearance of phases at temperatures below their stability range. In particular, there was a significant concentration of spinel (up to $\sim 2 \text{ wt}\%$) in the samples up to 50°C below the lower boundary of the spinel+hematite phase field ($(\text{MnO}_x)_n(\text{FeO}_y)_{(100-n)}$ where $n < 40$), as seen in the XRD pattern for $(\text{MnO}_x)_{20}(\text{FeO}_y)_{80}$ at 965°C in Fig. 2. The nonequilibrium spinel did not fully convert to the lower-temperature hematite+bixbyite phases even within heat-treatment times up to 262 h as samples were isothermally heat treated for different times to confirm that the spinel required extremely long times to convert to the lower temperature phases of bixbyite+hematite. The location of the low-temperature phase boundary of the hematite+bixbyite phase field was dictated by the temperatures at which bixbyite appeared.

Additional samples were measured by HSX, QF, DTA–TGA, and dilatometry. DTA–TGA was used to measure the spinel to spinel+hausmannite phase boundary. Figure 3 shows a DTA–TGA plot of temperature difference and weight as a function of temperature for pure MnO_x . The onset temperature of 1165°C indicates the boundary between hausmannite and the spinel phase field for this composition. In addition, HSX found that the phase boundary between spinel and spinel+hausmannite is between 1150° and 1160°C . These two methods agree reasonably well with one another to confirm the position of phase boundary in the phase diagram. Because of the ramp-heating operation of DTA/TGA, it was expected that the

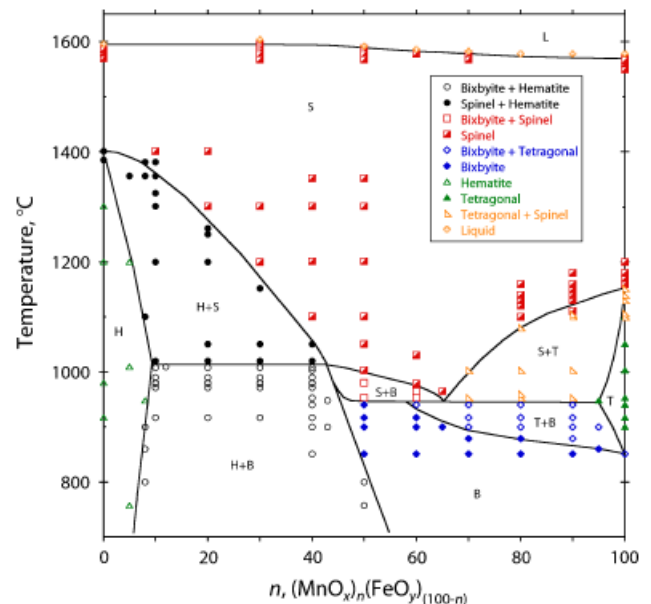


Fig. 1. $\text{MnO}_x\text{--FeO}_y$ binary phase diagram.

Table I. Summary of Heat-Treatment Results

Entry	Mn	Fe	Temperature (°C)	Ph
IHT	8	92	800	B,H
IHT	8	92	860	B,H
IHT	8	92	900	B,H
IHT	10	90	917	B,H
IHT	10	90	972	B,H
IHT	10	90	979	B,H
IHT	10	90	979	B,H
IHT	10	90	980	B,H
IHT	10	90	990	B,H,S
IHT	10	90	990	B,H,S
IHT	10	90	1008	B,H,S
IHT	12	88	1009	B,H
IHT	20	80	917	B,H
IHT	20	80	972	B,H
IHT	20	80	979	B,H
IHT	20	80	980	B,H
IHT	20	80	990	B,H,S
IHT	20	80	990	B,H,S
IHT	20	80	1008	B,H,S
IHT	30	70	917	B,H
IHT	30	70	972	B,H
IHT	30	70	979	B,H
IHT	30	70	980	B,H
IHT	30	70	990	B,H,S
IHT	30	70	990	B,H,S
IHT	30	70	1008	B,H,S
IHT	40	60	851	B,H
IHT	40	60	900	B,H
IHT	40	60	917	B,H
IHT	40	60	940	B,H
IHT	40	60	953	B,H,S
IHT	40	60	972	B,H,S
IHT	40	60	979	B,H
IHT	40	60	980	B,H
IHT	40	60	990	B,H,S
IHT	40	60	990	B,H,S
IHT	40	60	1003	B,H
IHT	40	60	1008	B,H,S
IHT	43	57	900	B,H
IHT	43	57	948	S,B,H
IHT	50	50	757	B,H
IHT	50	50	800	B,H
IHT	0	100	1401	S,H
DTA	0	100	1385	S,H
IHT	5	95	1356	S,H
DTA	5	95	1323	S,H
IHT	8	92	1100	S,H
IHT	8	92	1356	S,H
IHT	8	92	1381	S,H
IHT	10	90	1020	S,H
IHT	10	90	1200	S,H
IHT	10	90	1301	S,H
IHT	10	90	1356	S,H
IHT	10	90	1381	S,H
DTA	10	90	1325	S,H
IHT	20	80	1020	S,H
IHT	20	80	1051	H,S
IHT	20	80	1200	S,H
IHT	20	80	1250	S,H
DTA	20	80	1261	S,H
IHT	30	70	1020	S,H
IHT	30	70	1051	S,H
IHT	30	70	1152	S,H
IHT	40	60	1020	S,H
IHT	40	60	1051	S,H

(Continued)

Table I. Continued

Entry	Mn	Fe	Temperature (°C)	Ph
IHT	50	50	953	S,B
IHT	50	50	980	S,B
IHT	60	40	953	S,B
QF	60	40	965	S,B
IHT	60	40	940	B,T,S
IHT	70	30	900	B,T
IHT	70	30	917	B,T
IHT	70	30	940	B,T
IHT	80	20	900	B,T
IHT	80	20	917	B,T
IHT	80	20	940	B,T,S
IHT	90	10	879	B,T
IHT	90	10	900	B,T
IHT	90	10	917	B,T
IHT	90	10	940	B,T
IHT	95	5	900	B,T
IHT	100	0	851	B,T
IHT	95	5	948	T
IHT	100	0	900	T
IHT	100	0	917	T
IHT	100	0	940	T
IHT	100	0	953	T
IHT	100	0	1003	T
IHT	100	0	1051	T
IHT	100	0	1100	T
IHT	0	100	917	H
IHT	0	100	980	H
IHT	0	100	1200	H
IHT	0	100	1301	H
IHT	5	95	757	H
IHT	5	95	1009	H
IHT	5	95	1200	H
IHT	8	92	948	H
TMP/Pt	0	100	1586	S
IHT	10	90	1401	S
IHT	20	80	1301	S
IHT	20	80	1401	S
IHT	30	70	1200	S
IHT	30	70	1301	S
TMP/Al	30	70	1568	S
TMP/Pt	30	70	1568	S
QF	30	70	1570	S
TMP/Al	30	70	1578	S
TMP/Pt	30	70	1578	S
QF	30	70	1580	S
TMP/Al	30	70	1583	S
TMP/Pt	30	70	1583	S
TMP/Al	30	70	1588	S
TMP/Pt	30	70	1588	S
TMP/Al	30	70	1592	S
TMP/Pt	30	70	1592	S
TMP/Al	30	70	1596	S
TMP/Pt	30	70	1596	S
IHT	40	60	1100	S
IHT	40	60	1201	S
IHT	40	60	1301	S
IHT	40	60	1352	S
IHT	50	50	1003	S
IHT	50	50	1051	S
IHT	50	50	1100	S
IHT	50	50	1201	S
IHT	50	50	1301	S
IHT	50	50	1352	S
TMP/Al	50	50	1568	S
TMP/Pt	50	50	1568	S

(Continued)

Table I. Continued

Entry	Mn	Fe	Temperature (°C)	Ph
TMP/Al	50	50	1578	S
TMP/Pt	50	50	1578	S
TMP/Al	50	50	1583	S
TMP/Pt	50	50	1583	S
TMP/Al	50	50	1588	S
TMP/Pt	50	50	1588	S
QF	60	40	979	S
QF	60	40	1030	S
TMP/Pt	60	40	1578	S
IHT	65	35	965	S
TMP/Al	70	30	1568	S
TMP/Pt	70	30	1568	S
TMP/Al	70	30	1578	S
TMP/Pt	70	30	1578	S
HSX	80	20	1100	S
HSX	80	20	1120	S
HSX	80	20	1130	S
HSX	80	20	1140	S
HSX	80	20	1160	S
HSX	90	10	1110	S
HSX	90	10	1130	S
HSX	90	10	1140	S
HSX	90	10	1150	S
HSX	90	10	1160	S
HSX	90	10	1180	S
HSX	100	0	1160	S
HSX	100	0	1170	S
HSX	100	0	1180	S
HSX	100	0	1200	S
HSX	100	0	1550	S
HSX	100	0	1560	S
TMP/Pt	100	0	1566	S
IHT	70	30	953	T,S
IHT	70	30	1003	T,S
IHT	80	20	953	T,S
HSX	80	20	960	T,S
IHT	80	20	1003	T,S
HSX	80	20	1080	T,S
IHT	90	10	953	T,S
IHT	90	10	1003	T,S
IHT	90	10	1100	T,S
HSX	90	10	1105	T,S
HSX	100	0	1100	T,S
HSX	100	0	1106	T,S
HSX	100	0	1130	T,S
HSX	100	0	1140	T,S
HSX	100	0	1152	T,S
IHT	50	50	851	B
IHT	50	50	900	B
IHT	50	50	917	B
IHT	50	50	940	B
IHT	60	40	851	B
IHT	60	40	900	B
IHT	60	40	917	B
IHT	65	35	900	B
IHT	70	30	851	B
IHT	70	30	879	B
IHT	80	20	851	B
IHT	80	20	879	B
IHT	90	10	851	B
IHT	95	5	860	B
TMP/Pt	0	100	1596	Liq
TMP/Pt	30	70	1604	Liq
TMP/Al	30	70	1604	Liq
TMP/Pt	50	50	1592	Liq

(Continued)

Table I. Continued

Entry	Mn	Fe	Temperature (°C)	Ph
TMP/Al	50	50	1592	Liq
TMP/Pt	60	40	1586	Liq
TMP/Pt	70	30	1583	Liq
TMP/Al	70	30	1583	Liq
TMP/Al	80	20	1578	Liq
TMP/Al	90	10	1578	Liq
TMP/Pt	100	0	1578	Liq

The method used to determine the value presented is listed under “Entry” where HSX, hot-stage XRD; IHT, isothermal heat treatment; QF, quench furnace; DTA, differential thermal and thermogravimetric analysis; TMP/Al, melting point evaluation using Al₂O₃ crucible; TMP/Pt, melting point evaluation using platinum crucible; XRD, X-ray diffraction. MnO_x and FeO_y compositions are listed in mass%. Phases identified, listed as “Ph.” are bixbyite (B), spinel (S), hausmannite, or tetragonal (T), hematite (H), or mixtures of these.

boundary would appear at a higher temperature than the HSX results. Therefore, the DTA/TGA results confirm HSX measurements that are considered representative of equilibrium.

Dilatometry was used for one sample, (MnO_x)₈₀(FeO_y)₂₀, to help determine the boundary between spinel and spinel+hausmannite. For (MnO_x)₈₀(FeO_y)₂₀, the change from the hausmannite+spinel phase field to the spinel field occurs at a temperature of 1107°C as the sample changes from expansion to shrinkage. The shrinkage is a result of the sample converting from the lower density tetragonal structure (ρ_{hausmannite} = 4.84 g/cm³) of hausmannite, with an elongated *c*-axis to the higher density cubic structure (ρ_{jacobsite} = 4.87 g/cm³) of spinel with equal axes.⁹ Water quenching the IHT samples successfully suppressed the reversion of spinel to hausmannite upon cooling for compositions near the eutectoid formed between the hausman-

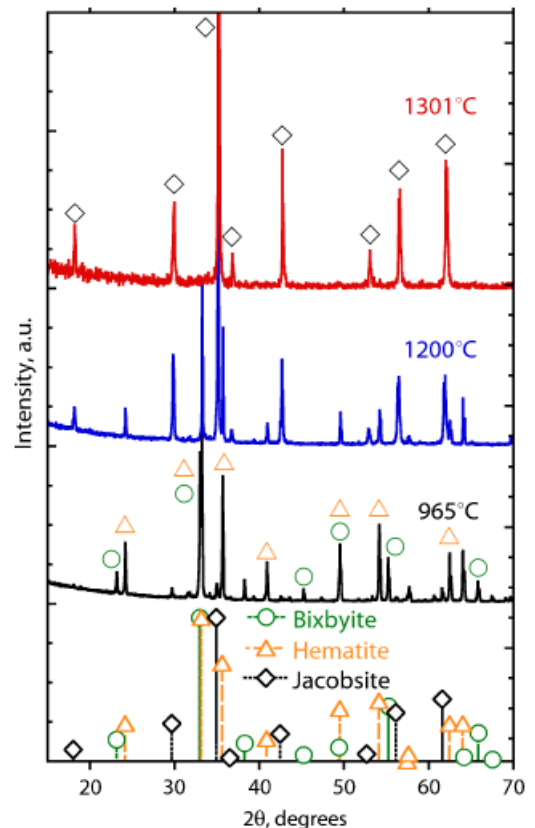


Fig. 2. X-ray diffraction patterns (MnO_x)₂₀(FeO_y)₈₀ in the spinel (1301°C, 24 h), spinel+hematite (1200°C, 24 h), and bixbyite+hematite (965°C, 262 h) phase fields.

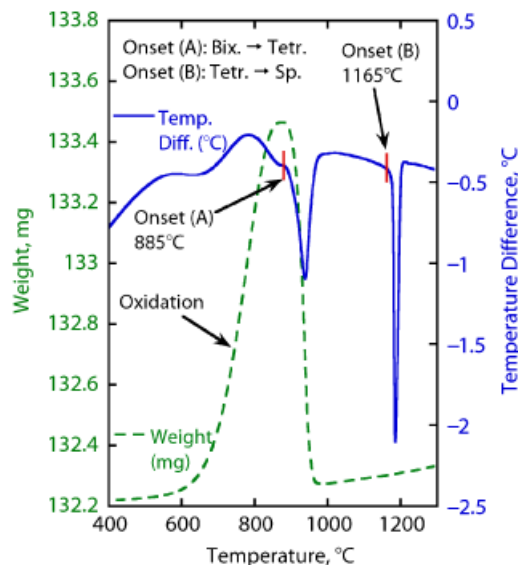


Fig. 3. Differential thermal analysis/thermogravimetric analysis analysis of Mn_2O_3 in air at a heating rate of $10^\circ\text{C}/\text{min}$.

nite+spinel phase field and the spinel+bixbyite phase field. At higher concentrations of MnO_x , water quenching was not sufficient to avoid the reversion from spinel to hausmannite.

Table II compares the temperatures that separate the spinel phase field from the hausmannite+spinel phase field for the HSX, DTA–TGA, and dilatometry methods as well as data from Van Hook.² IHT data were not included in Table II because of spinel reverting to hausmannite upon cooling. The HSX data show that the phase boundary occurs at temperatures similar to the data in the literature,³ whereas the DTA–TGA data appear to be up to $\sim 20^\circ\text{C}$ higher. Both methods show reasonable agreement in regard to the data trends. The data also indicate limitations for both methods. The HSX and DTA–TGA produced good results for the 100 wt% MnO_x composition. Measurements were more difficult to collect for samples with increasing FeO_y . The DTA–TGA method was limited by the decreasing signal for the temperature difference that indicates the reaction. The HSX was less affected by the decreasing signal but it was also impacted by the increasing concentration of FeO_y . For this reason, the dilatometry and QF methods were used to confirm the upper boundary for regions of the hausmannite+spinel phase field rich in FeO_y ; as the results in Table II indicate, this phase field required several methods to accurately determine the upper boundary.

IV. Discussion

Generally, Fig. 1 agrees fairly well with the diagram by Muan and Somiya.³ However, the start of the spinel+hausmannite phase field for the Muan and Somiya³ diagram is at 70 wt% Mn_2O_3 , whereas the present study indicates that the boundary is near 65 wt% Mn_2O_3 . The Muan and Somiya³ diagram indicated

Table II. Comparison of Hausmannite-to-Spinel-Transformation Temperatures Measured by Hot-Stage XRD, Dilatometer, and DTA/TGA for the Hausmannite to Spinel Phase Change

Mn_2O_3	Fe_2O_3	Hot-stage XRD	DTA/TGA	Dilatometer
100	0	1162°C	1167°C (2°C/min)	
100	0	1156°C	1165°C	—
90	10	1105°C	1150°C	—
80	20	1080°C	1111°C (10°C/min)	1107°C

Data from Van Hook *et al.*² is included on the top line for comparison purposes. XRD, X-ray diffraction; DTA, differential thermal analysis; TGA, thermogravimetric analysis.

the spinel to spinel+hausmannite phase boundary as speculative. Van Hook *et al.*² gathered data at 900°C , with a CO_2/CO atmospheric ratio of 300, that bracketed the appearance of a tetragonal phase between 60 and 70 wt% Mn_3O_4 . Cervinka *et al.*^{4,5} defined the cubic–tetragonal distortion boundary to be within a compositional range of 64.3 and 65.5 wt% Mn_2O_3 . The present study agrees well with the boundary determination of Cervinka and Van Hook.^{2,4,5} In the present study, spinel was not stable in compositions >65 wt% Mn_2O_3 , and partially or fully reverted to the hausmannite phase upon cooling. The boundary was measured with HSX, DTA–TGA, and water-quenched samples, as mentioned and described above. The combination of methods provided an accurate and self consistent determination of the boundary between spinel and spinel+hausmannite.

Figure 4 shows the different data collected in the spinel, hematite, spinel+hematite, and hematite+bixbyite phase fields. IHT and DTA–TGA methods were used collectively to determine the boundary locations between spinel and spinel+hematite and between the spinel+hematite and hematite+bixbyite phase fields. Since the IHT data alone were insufficient to determine these boundaries.

In regards to the upper boundary of the spinel and spinel+hematite phase fields, IHT samples with <10 wt% Mn_2O_3 retain hematite at temperatures higher than expected well into the spinel phase field. The DTA–TGA method provided the additional data needed to accurately determine this boundary. Additionally, data collected using the DTA–TGA method agree well with all of the IHT samples containing at ≥ 20 wt% MnO_x .

At the lower boundary of the spinel+hematite phase field as seen in Fig. 4, bixbyite appeared in IHT samples at temperatures of up to 1015°C in combination with hematite and a small fraction of spinel. DTA–TGA method results indicate that the transition from the hematite+bixbyite phase field to the spinel+hematite phase field occurs at $\sim 980^\circ\text{C}$. The presence of all three phases between 1015° and 980°C indicates that the samples have not reached equilibrium. For this reason additional IHT samples were heat treated between the temper-

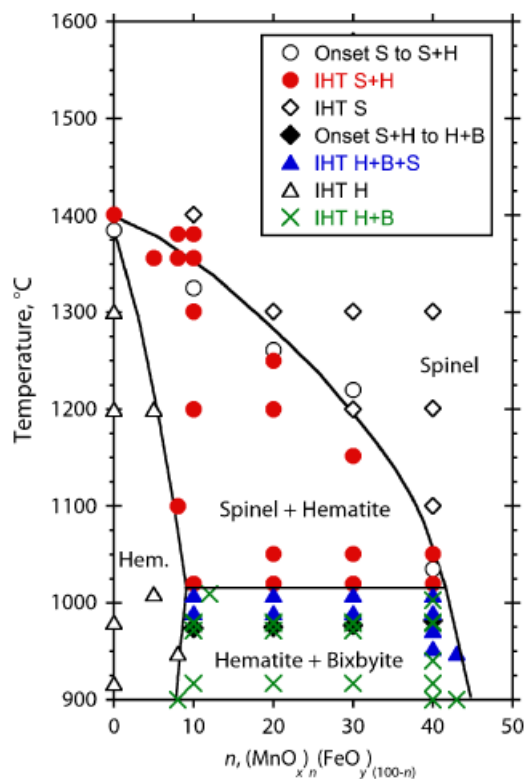


Fig. 4. Isothermal heat treatment (IHT) and onset data plotted versus concentration on high FeO_y side of diagram.

atures of 8980° and 1015°C for times up to 262 h to verify that equilibrium was reached. As heat-treatment times were increased, the fraction of spinel outside of the hematite+bixbyite phase field decreased accordingly but a small fraction of spinel remained present regardless of the time of testing. In order to achieve a spinel-free sample, heat-treatment times would need to be significantly longer than 262 h.

All other phase data used to construct the phase diagram were measured with IHT. The spinel phase field is continuous from 100 wt% FeO_y to 100 wt% MnO_x up to the melting point of the solid mixtures, which ranges from 1597°C at 100 wt% FeO_y down to 1573°C at 100 wt% MnO_x. The hematite phase field begins at 1401°C and extends to 750°C. The hematite+spinel phase field also begins at 1401°C. As the concentration of MnO_x is increased up to ~42 wt%, the phase boundary between spinel and hematite+spinel lowers from 1401°C to a minimum of ~1010°C. At 1010°C there is a eutectoid between spinel, spinel+hematite, and spinel+bixbyite. The spinel+bixbyite phase field extends down to another eutectoid point between spinel, spinel+bixbyite, and spinel+hausmannite (tetragonal) at a temperature of 948°C. The spinel+hausmannite (tetragonal) phase field extends from 1160°C at 100 wt% MnO_x down to 948°C at 65 wt% MnO_x.

Below these phase fields, spinel is no longer stable because of the oxidation state of Fe and Mn. Both begin to convert to the 3+ oxidation state. Fe₃O₄ converts to Fe₂O₃ at a maximum of 1401°C at 100 wt% FeO_y. Mixtures of Mn₃O₄ and Fe₃O₄ convert to Mn₂O₃ and Fe₂O₃ anywhere from 1401°C at 100 wt% FeO_y down to the minimum of 851°C at 100 wt% MnO_x.

V. Diagram Comparisons

The diagram given in Fig. 1 is similar to the diagram given by Muan and Somiya³ and all of the phase fields appear relatively close. However, the boundaries have few differences that were worth examining. Figure 5 shows a close-up of the phase boundary between spinel and spinel+hausmannite for this study and

data presented by Muan and Somiya.³ The boundary determined in this study is measured consistently while that reported by Muan and Somiya³ was reported as uncertain or “speculative.” Figure 5 shows a difference in the location of the spinel-to-spinel+hausmannite phase boundary and the location of the eutectoid. The availability of HSX for this study has generated significantly more data in the spinel phase field above the spinel+hausmannite phase field and defined the placement of the boundary in comparison to the data available in the Muan and Somiya³ diagram. The eutectoid where spinel+bixbyite, spinel, and spinel+hausmannite phase fields intersect was determined to be at 65 wt% Mn₂O₃ for this study whereas the Muan and Somiya³ diagrams indicate it to be at 70 wt% Mn₂O₃. Cervinka *et al.*^{4,5} determined the boundary between spinel and tetragonal distorted hausmannite to be between 64 and 65.5 wt% Mn₂O₃. These differences are not surprising considering the difficulty associated with suppressing reversion of spinel to hausmannite upon cooling in the spinel phase field above the spinel+hausmannite phase field. The spinel+bixbyite to spinel phase boundary agree well with the Muan and Somiya³ diagram.

The liquid-to-spinel phase boundary presented here shows minor differences from the data presented by Muan and Somiya³ as seen in Fig. 6. Generally, the data in this study indicate that the boundary is approximately 10°C higher than that presented by Muan and Somiya.³ The Muan and Somiya data define the boundary well within the composition region of 62.5–100 wt% Mn₂O₃. However, the boundary appears to be extrapolated to the iron end member of the diagram as there is no liquid phase data given for compositions with Fe₂O₃ concentrations >60 wt%. The data from this study agree well with the extrapolation of the spinel-to-liquid phase boundary at the iron end member. Additionally, both sets of data agree well with melting points provided in the literature for the end members of the diagram.⁹ As seen in Table I, the data collected for heat treatment evaluations run in Al₂O₃ (TMP/Al) and Pt (TMP/Pt) crucibles agree within the 5°–10°C upper and lower temperatures used to bracket liquidus boundary hence the fact that

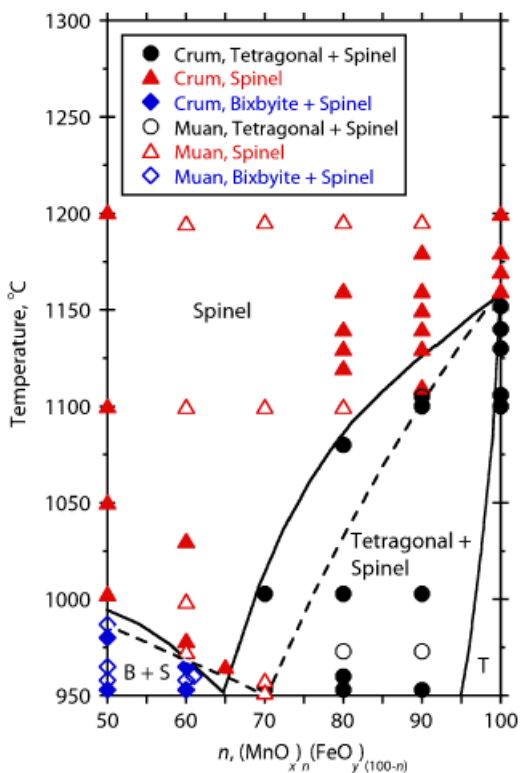


Fig. 5. Comparison plot of spinel+hausmannite (tetragonal) to spinel boundary with data from Muan and Somiya³ (dashed line).

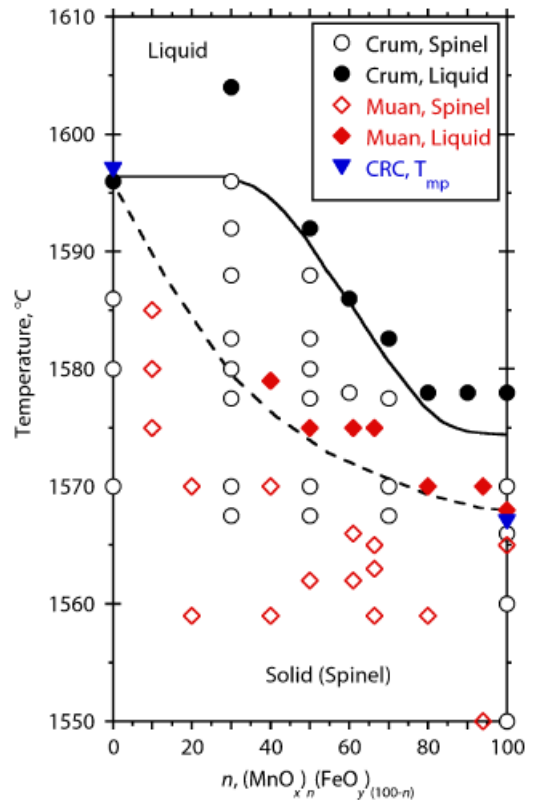


Fig. 6. Liquid-to-spinel phase boundary comparison with Muan and Somiya³ (dashed line).

samples melted in Al_2O_3 crucibles did partially dissolve into the crucible (as per SEM/EDS), the effect on the melting temperatures for each compound tested was negligible.

VI. Conclusions

A self consistent phase diagram for the MnO_x - FeO_y system in air was generated and compared with previously reported diagrams. It was found that rapid phase transformations from spinel to haussmannite in the compositions >65 wt% MnO_x and $>950^\circ\text{C}$ made it difficult to identify this phase boundary. A series of analytical techniques were used to clearly and consistently identify this phase boundary. The phase diagram reported in this paper also updates the liquid to spinel boundary found in literature.^{3,9}

A regimen for measuring phase diagrams with changing oxidation states and rapid phase transformations was reported. The combinations of these methods should be generally applicable to the measurement of other phase diagrams/phase field boundaries that have been uncertainly estimated in previous literature. By consistently applying these methods, key areas of existing ceramic phase diagrams can be refined and updated for application in thermodynamic modeling and technological applications.

Acknowledgment

This work was performed for the Environmental Management Science Program. Authors would like to thank Dave McCready for helpful discussions and for performing the HSX measurements.

References

- ¹T. M. Besmann, N. S. Kulkarni, K. E. Spear, and J. D. Vienna, "Predicting Phase Equilibria of Spinel-Forming Constituents in Waste Glass Systems"; pp. 121–31 in *Ceramic Transactions*, Vol. 168. American Ceramic Society, Indianapolis, IN, 2004.
- ²H. J. Van Hook and M. L. Keith, "The System Fe_3O_4 - Mn_3O_4 ," *Am. Mineral.*, **43**, 69–83 (1958).
- ³A. Muan and S. Somiya, "System Iron Oxide–Manganese Oxide in Air," *Am. J. Sci.*, **260** [3] 230–40 (1962).
- ⁴L. Cervinka, "On the existence of Tetragonally Deformed Octahedrons in the Cubic Part of the System $\text{Mn}_x\text{Fe}_{3-x}\text{O}_4$," *Czech. J. Phys. Sect. B*, **15** [10] 747–51 (1965).
- ⁵L. Cervinka, R. Hosemann, and W. Vogel, "Paracrystalline Lattice Distortions and Microdomains in Manganese Ferrites Near the Cubic-to-Tetragonal Transition," *Acta Cryst.*, **A26** [2] 277–89 (1970).
- ⁶H. F. McMurdie, B. M. Sullivan, and F. A. Mauer, "High-Temperature X-Ray Study of the System Fe_3O_4 - Mn_3O_4 ," *J. Res. NBS*, **45**, 35–41 (1950).
- ⁷P. Holba, M. A. Khilla, and S. Krupika, "On the Miscibility Gap of Spinel $\text{Mn}_x\text{Fe}_{3-x}\text{O}_4$," *J. Phys. Chem. Solids*, **34**, 387–95 (1973).
- ⁸W. D. Kingery, H. K. Bowen, and D. R. Uhlmann, *Introduction to Ceramics*, 2nd edition, John Wiley & Sons, New York, 1976.
- ⁹D. Lide, *CRC Handbook of Chemistry and Physics*, 88th edition, CRC press, Boca Raton, FL, 2007–2008. □